

NASA Contractor Report 178273

ICASE REPORT NO. 87-20

ICASE

TOWARD THE LARGE-EDDY SIMULATIONS OF
COMPRESSIBLE TURBULENT FLOWS
(NASA-CR-178273) TOWARD THE LARGE-EDDY
SIMULATIONS OF COMPRESSIBLE TURBULENT FLOWS
Final Report (NASA) 39 p CSCL 20D

N87-21259

Unclas

G3/34 43563

G. Eriebacner

M. Y. Hussaini

C. G. Speziale

T. A. Zang

Contract No. NAS1-18107

March 1987

INSTITUTE FOR COMPUTER APPLICATIONS IN SCIENCE AND ENGINEERING
NASA Langley Research Center, Hampton, Virginia 23665

Operated by the Universities Space Research Association



National Aeronautics and
Space Administration

Langley Research Center
Hampton, Virginia 23665

TOWARD THE LARGE-EDDY SIMULATION OF COMPRESSIBLE TURBULENT FLOWS

G. Erlebacher

NASA Langley Research Center

M. Y. Hussaini

Institute for Computer Applications in Science and Engineering

C. G. Speziale

Georgia Institute of Technology

T.A. Zang

NASA Langley Research Center

New subgrid-scale models for the large-eddy simulation of compressible turbulent flows are developed based on the Favre-filtered equations of motion for an ideal gas. A compressible generalization of the linear combination of the Smagorinsky model and scale-similarity model (in terms of Favre-filtered fields) is obtained for the subgrid-scale stress tensor. An analogous thermal linear combination model is also developed for the subgrid-scale heat flux vector. The three dimensionless constants associated with these subgrid-scale models are obtained by correlating with the results of direct numerical simulations of compressible isotropic turbulence performed on a 96^3 grid using Fourier collocation methods. Extensive comparisons between the direct and modeled subgrid-scale fields are provided in order to validate the models. Future applications of these compressible subgrid-scale models to the large-eddy simulation of supersonic aerodynamic flows are discussed briefly.

Research for the second and third authors was supported under the National Aeronautics and Space Administration under NASA Contract No. NAS1-18107 while in residence at the Institute for Computer Applications in Science and Engineering (ICASE) NASA Langley Research Center, Hampton, VA 23665.

1. Introduction

The direct numerical simulation of turbulent flows at the high Reynolds numbers encountered in problems of technological importance is all but impossible as a result of the wide range of scales that are present. Consequently, the solutions to such problems must invariably be based on some form of turbulence modeling. Traditional turbulence models based on Reynolds averages have had only limited success since the large scales of the turbulence (which contain most of the energy) are highly dependent on the geometry of the flow being considered. Experience has indicated that such models usually break down when a variety of turbulent flows are considered (Lumley 1983). The small scales are more universal in character, and serve mainly as a source for dissipation. Hence, it can be argued that a better understanding of turbulent flows could be achieved if just the small scales are modeled while the large scales are calculated (Deardorff 1970). This is the fundamental idea behind large-eddy simulations.

During the past decade, considerable progress has been made in the large-eddy simulation of incompressible turbulent flows. This effort has shed new light on the physics of turbulence. The earliest work relied heavily on the use of the Reynolds averaging assumption to eliminate the Leonard and cross stresses while the Reynolds stresses were computed using the Smagorinsky model (Deardorff 1970, Leonard 1974, Reynolds 1976). More recent large-eddy simulations have been based on the direct calculation of the Leonard stresses with models provided for the cross and Reynolds subgrid-scale stresses in order to enhance the numerical accuracy (see Biringen and Reynolds 1981, Bardina Ferziger and Reynolds 1983). However, among these models, only the particular Bardina, Ferziger and Reynolds (1983) model, with a Bardina constant of 1.0, satisfies the important physical constraint of Galilean invariance (Speziale 1985). The underlying physical concepts, fundamental numerical algorithms, and comprehensive historical data behind the recent field of large-eddy simulation have been presented in articles by Schumann (1975), Voke and Collins (1983) and Rogallo and Moin (1984).

Despite the intensive research effort that has been devoted to the large-eddy simulation of incompressible flows as outlined above, it appears that no large-eddy simulation of a compressible turbulent flow has yet been attempted. Of course, such work could have important technological applications in the analysis of turbulent supersonic flows where shock waves are generated and in turbulent flows in combustion chambers. The prerequisite for carrying out such computations is the development of suitable subgrid-scale models for compressible turbulent flows. With the exception of the recent work of Yoshizawa (1986) few, if any, studies along these lines appear to have been published. The subgrid-scale models of Yoshizawa are only suitable for slightly compressible turbulent flows since they made use of an asymptotic expansion about an incompressible state. Hence, there is a need for subgrid-scale models that can be applied to the study of turbulent flows which are strongly compressible (i.e. for Mach numbers $M > 1$ where shock waves can occur). This forms the *raison d'être* for the present study.

In this paper, subgrid-scale models will be developed for the closure of the Favre-filtered Navier-Stokes and energy equations. The compressible subgrid-scale stress model that will be obtained in Section 2 reduces to the linear combination model of Bardina, Ferziger and Reynolds (1983) in the incompressible limit. Likewise, the subgrid-scale heat flux model that will be obtained herein consists of an analogous linear combination of scale similarity and gradient transport terms. The dimensionless constants which appear in these subgrid-scale models will be arrived at by correlating with the results of direct numerical simulations of compressible isotropic turbulence. A more detailed comparison of computed and modeled subgrid-scale fields will be presented along with a discussion of the prospects for future research.

2. Subgrid-Scale Models for Compressible Turbulence

The compressible turbulent flow of an ideal gas will be considered. Such flows are governed by the continuity, momentum and energy equations given by (Batchelor 1967)

$$\frac{\partial \rho}{\partial t} + \frac{\partial(\rho v_k)}{\partial x_k} = 0 \quad (1)$$

$$\frac{\partial(\rho v_k)}{\partial t} + \frac{\partial(\rho v_k v_l)}{\partial x_l} = -\frac{\partial p}{\partial x_k} + \frac{\partial \sigma_{kl}}{\partial x_l} \quad (2)$$

$$\frac{\partial(\rho h)}{\partial t} + \frac{\partial(\rho h v_k)}{\partial x_k} = \frac{\partial p}{\partial t} + v_k \frac{\partial p}{\partial x_k} + \frac{\partial}{\partial x_k} \left(\kappa \frac{\partial T}{\partial x_k} \right) + \Phi \quad (3)$$

respectively, where ρ is the mass density, \mathbf{v} is the velocity vector, p is the thermodynamic pressure, μ is the dynamic viscosity, h is the enthalpy, T is the absolute temperature, and κ is the thermal conductivity. The viscous stress σ_{kl} and the viscous dissipation Φ are respectively defined by

$$\sigma_{kl} = -\frac{2}{3}\mu \frac{\partial v_j}{\partial x_j} \delta_{kl} + \mu \left(\frac{\partial v_k}{\partial x_l} + \frac{\partial v_l}{\partial x_k} \right) \quad (4)$$

$$\Phi = -\frac{2}{3}\mu \left(\frac{\partial v_j}{\partial x_j} \right)^2 + \mu \left(\frac{\partial v_k}{\partial x_l} + \frac{\partial v_l}{\partial x_k} \right) \frac{\partial v_k}{\partial x_l} \quad (5)$$

The Einstein summation convention applies to repeated indices and the effects of external body forces have been neglected for simplicity. Equations (1)-(3) must be supplemented with the equations of state for an ideal gas which are as follows:

$$P = \rho RT, \quad h = C_p T \quad (6)$$

where R is the ideal gas constant and C_p is the specific heat at constant pressure. Likewise, the dependence of the viscosity and thermal conductivity on the temperature must be provided (i.e., relationships of the form $\mu = \mu(T)$ and $\kappa = \kappa(T)$ are needed and these depend on the gas under study).

Any flow variable \mathcal{F} can be filtered in the following manner:

$$\bar{\mathcal{F}}(\mathbf{x}) = \int_D G(\mathbf{x} - \mathbf{z}, \Delta) \mathcal{F}(\mathbf{z}) d^3z \quad (7)$$

where G is a filter function, Δ is the computational mesh size, and D is the domain of the fluid. The filter function G can either be an infinitely differentiable function of bounded support in an arbitrary domain, or a Gaussian distribution in a periodic domain[†]. It is normalized by requiring that

$$\int_D G(\mathbf{x} - \mathbf{z}, \Delta) d^3z = 1. \quad (8)$$

It follows that in the limit as the computational mesh size goes to zero, (7) becomes a Dirac delta sequence, i.e.

$$\lim_{\Delta \rightarrow 0} \int_D G(\mathbf{x} - \mathbf{z}, \Delta) \mathcal{F}(\mathbf{z}) d^3z = \int_D \delta(\mathbf{x} - \mathbf{z}) \mathcal{F}(\mathbf{z}) d^3z = \mathcal{F}(\mathbf{x}) \quad (9)$$

where $\delta(\mathbf{x} - \mathbf{z})$ is the Dirac delta function (Arfken 1970). As a direct result of the Riemann-Lebesgue theorem, (7) substantially reduces the amplitude of the high-frequency spatial Fourier components of any flow variable \mathcal{F} . Consequently, $\bar{\mathcal{F}}$ can be more accurately termed the large-scale part of \mathcal{F} . At this point, it should be mentioned that as a result of the defining properties of G , it follows that

$$\frac{\partial \bar{\mathcal{F}}}{\partial t} = \overline{\frac{\partial \mathcal{F}}{\partial t}}, \quad \frac{\partial \bar{\mathcal{F}}}{\partial x_k} = \overline{\frac{\partial \mathcal{F}}{\partial x_k}}. \quad (10)$$

The turbulent fields are decomposed as follows, based on Favre filtering,

$$\mathcal{F} = \tilde{\mathcal{F}} + \mathcal{F}' \quad (11)$$

where the Favre filter

$$\tilde{\mathcal{F}} = \frac{\overline{\rho \mathcal{F}}}{\bar{\rho}} \quad (12)$$

is defined in an analogous manner to the Favre time average which has been of use in the more traditional studies of compressible turbulent flows (Hinze 1975). However, contrary to the more traditional Favre time averaging,

$$\tilde{\tilde{\mathcal{F}}} \neq \tilde{\mathcal{F}} \quad (13)$$

in general, and hence

$$\tilde{\mathcal{F}}' \neq 0. \quad (14)$$

The direct filtering of the continuity equation (1) yields

$$\frac{\partial \bar{\rho}}{\partial t} + \frac{\partial (\bar{\rho} \tilde{v}_k)}{\partial x_k} = 0 \quad (15)$$

[†] A Gaussian filter is adopted for the calculations in this study

where we have used (10) and (12). Likewise, a direct filtering of the momentum equation yields

$$\frac{\partial(\bar{\rho}\tilde{v}_k)}{\partial t} + \frac{\partial(\bar{\rho}\tilde{v}_k\tilde{v}_l)}{\partial x_l} = -\frac{\partial\bar{p}}{\partial x_k} + \frac{\partial\bar{\sigma}_{kl}}{\partial x_l} + \frac{\partial\tau_{kl}}{\partial x_l} \quad (16)$$

where

$$\bar{p} = \bar{\rho}R\tilde{T} \quad (17)$$

$$(18)$$

and

$$\tau_{kl} = -\bar{\rho}(\widetilde{\tilde{v}_k\tilde{v}_l} - \tilde{v}_k\tilde{v}_l + \widetilde{v'_k\tilde{v}_l} + \widetilde{v'_l\tilde{v}_k} + \widetilde{v'_kv'_l}) \quad (19)$$

is the subgrid-scale stress tensor. The subgrid-scale stress tensor can be decomposed as follows,

$$\tau = \mathbf{L} + \mathbf{C} + \mathbf{R} \quad (20)$$

where

$$L_{kl} = -\bar{\rho}(\widetilde{\tilde{v}_k\tilde{v}_l} - \tilde{v}_k\tilde{v}_l) \quad (21)$$

$$C_{kl} = -\bar{\rho}(\widetilde{v'_k\tilde{v}_l} + \widetilde{v'_l\tilde{v}_k}) \quad (22)$$

$$R_{kl} = -\bar{\rho}\widetilde{v'_kv'_l} \quad (23)$$

are respectively, the subgrid-scale Leonard, cross, and Reynolds stresses based on Favre filtering. From (21), it is clear that the Leonard stress can be calculated directly and does not need to be modeled. The cross stress is modeled with the Galilean invariant scale similarity model

$$C_{kl} = -\bar{\rho}(\tilde{v}_k\tilde{v}_l - \tilde{\tilde{v}}_k\tilde{\tilde{v}}_l) \quad (24)$$

which is analogous to its incompressible counterpart which has been reasonably successful in the large-eddy simulation of incompressible turbulent flows (Bardina, Ferziger and Reynolds 1983, Speziale 1985). The subgrid-scale Reynolds stress tensor is separated into deviatoric and isotropic parts, respectively, as follows:

$$\mathbf{R} = {}_D\mathbf{R} + {}_I\mathbf{R} \quad (25)$$

where

$${}_D R_{kl} = -\bar{\rho}(\widetilde{v'_kv'_l} - \frac{1}{3}\widetilde{v'_i v'_i} \delta_{kl}), \quad (26)$$

and

$${}_I R_{kl} = -\frac{1}{3}\bar{\rho}\widetilde{v'_i v'_i} \delta_{kl}. \quad (27)$$

Here, the deviatoric part of the subgrid-scale Reynolds stress tensor, ${}_D\mathbf{R}$, is modeled using the compressible generalization of the Smagorinsky model that is given by

$${}_D R_{kl} = 2C_R \bar{\rho} \Delta^2 I \tilde{I}_{\tilde{S}}^{1/2} (\tilde{S}_{kl} - \frac{1}{3}\tilde{S}_{mm} \delta_{kl}) \quad (28)$$

where

$$\tilde{S}_{kl} = \frac{1}{2} \left(\frac{\partial \tilde{v}_k}{\partial x_l} + \frac{\partial \tilde{v}_l}{\partial x_k} \right) \quad (29)$$

$$II_{\tilde{S}} = \tilde{S}_{mn} \tilde{S}_{mn} \quad (30)$$

(i.e., \tilde{S} is the Favre filtered rate of strain tensor while $II_{\tilde{S}}$ is its second invariant) and C_R is the compressible Smagorinsky constant. The isotropic part of the subgrid-scale Reynolds stress tensor, ${}_I R$, is modeled by

$${}_I R_{kl} = -\frac{2}{3} C_I \bar{\rho} \Delta^2 II_{\tilde{S}} \delta_{kl} \quad (31)$$

where C_I is a dimensionless constant. Equation (31) can, for the most part, be obtained by making a turbulence production equals dissipation hypothesis (Yoshizawa 1986). Hence, the overall subgrid-scale stress model we propose takes the form

$$\begin{aligned} \tau_{kl} = & -\bar{\rho}(\tilde{v}_k \tilde{v}_l - \tilde{v}_k \tilde{v}_l) + 2C_R \bar{\rho} \Delta^2 II_{\tilde{S}}^{1/2} (\tilde{S}_{kl} - \frac{1}{3} \tilde{S}_{mm} \delta_{kl}) \\ & - \frac{2}{3} C_I \bar{\rho} \Delta^2 II_{\tilde{S}} \delta_{kl}. \end{aligned} \quad (32)$$

In the incompressible limit, the deviatoric part of (32) (which is all that is of consequence in an incompressible flow since the isotropic part can be absorbed into the pressure) reduces to the linear combination model

$$-{}_D \tau_{kl} / \rho = {}_D (\bar{v}_k \bar{v}_l - \bar{v}_k \bar{v}_l) - 2C_R \Delta^2 II_{\tilde{S}}^{1/2} \bar{S}_{kl} \quad (33)$$

of Bardina, Ferziger, and Reynolds (1983) where the Bardina constant is one in order to satisfy Galilean invariance (Speziale 1985). This follows from (32) since, for constant values of ρ ,

$$\tilde{\mathbf{v}} = \nabla, \quad \tilde{S}_{mm} = \bar{S}_{mm} = 0 \quad (34)$$

A direct filtering of the energy equation yields the filtered form

$$\begin{aligned} C_p \left[\frac{\partial(\bar{\rho} \tilde{T})}{\partial t} + \frac{\partial(\bar{\rho} \tilde{v}_k \tilde{T})}{\partial x_k} \right] = & \frac{\partial \bar{p}}{\partial t} + \bar{v}_k \frac{\partial \bar{p}}{\partial x_k} + \bar{\Phi} \\ & + \frac{\partial}{\partial x_k} \left(\kappa \frac{\partial \bar{T}}{\partial x_k} \right) - \frac{\partial Q_k}{\partial x_k} \end{aligned} \quad (35)$$

where

$$Q_k = C_p \bar{\rho} (\tilde{v}_k \tilde{T} - \tilde{v}_k \tilde{T} + \tilde{v}_k' \tilde{T} + \tilde{v}_k \tilde{T}' + \tilde{v}_k' \tilde{T}') \quad (36)$$

is the subgrid-scale heat flux. The subgrid-scale heat flux can be decomposed similarly to the decomposition of the subgrid-scale stresses. This leads to

$$\mathbf{Q} = \mathbf{Q}^{(L)} + \mathbf{Q}^{(C)} + \mathbf{Q}^{(R)} \quad (37)$$

where

$$Q^{(L)} = C_p \bar{\rho} (\widetilde{\tilde{v}_k \tilde{T}} - \tilde{v}_k \tilde{T}) \quad (38)$$

$$Q^{(C)} = C_p \bar{\rho} (\widetilde{v'_k \tilde{T}} + \tilde{v}_k \tilde{T}') \quad (39)$$

$$Q^{(R)} = C_p \bar{\rho} \widetilde{v'_k \tilde{T}'} \quad (40)$$

are the Leonard, cross, and Reynolds heat fluxes. Analogous to the modeling of the cross stresses, the cross heat flux is modeled using the scale similarity format

$$Q_k^{(C)} = C_p \bar{\rho} (\tilde{v}_k \tilde{T} - \tilde{\tilde{v}}_k \tilde{\tilde{T}}) \quad (41)$$

which is Galilean invariant. The Reynolds heat flux is modeled with the usual gradient transport format as follows (cf. Eidson 1985)

$$\widetilde{v'_k \tilde{T}'} = -C_T \Delta^2 II_{\tilde{s}}^{1/2} \frac{\partial \tilde{T}}{\partial x_k} \quad (42)$$

where C_T is a dimensionless constant such that

$$C_T = \frac{1}{Pr_T} C_R \quad (43)$$

given that Pr_T is the turbulent Prandtl number. Of course, the Leonard heat flux can be calculated directly. Hence, the overall model for the subgrid-scale heat flux we propose is

$$Q_k = C_p \bar{\rho} [(\widetilde{\tilde{v}_k \tilde{T}} - \tilde{\tilde{v}}_k \tilde{\tilde{T}}) - C_T \Delta^2 II_{\tilde{s}}^{1/2} \frac{\partial \tilde{T}}{\partial x_k}], \quad (44)$$

which is obtained by combining (38), (41) and (42).

At this point, some comments need to be made concerning the viscous terms on the right-hand side of (15) and the pressure gradient-velocity and viscous dissipation terms which appear on the right-hand side of (35). For high Reynolds number turbulent flows that are sufficiently far from solid boundaries and are not in the hypersonic regime (the only cases that are considered for this initial study), the viscous terms described above can be neglected. The pressure gradient-velocity correlation can be written in the alternative form

$$\begin{aligned} \overline{v_k \frac{\partial p}{\partial x_k}} &= \frac{\partial (\overline{p v_k})}{\partial x_k} - \overline{p \frac{\partial v_k}{\partial x_k}} \\ &= \frac{\partial (\overline{\rho R T v_k})}{\partial x_k} - \overline{\rho R T \frac{\partial v_k}{\partial x_k}} \\ &= R \frac{\partial (\overline{\tilde{p} \tilde{v}_k \tilde{T}})}{\partial x_k} + \frac{R}{C_p} \frac{\partial Q_k}{\partial x_k} - \overline{\tilde{p} R (T \frac{\partial \tilde{v}_k}{\partial x_k})} \end{aligned} \quad (45)$$

where only the pressure dilatation term

$$\overline{p \frac{\partial v_k}{\partial x_k}} = \overline{\tilde{p} R (T \frac{\partial \tilde{v}_k}{\partial x_k})} \quad (46)$$

is not yet closed. This pressure dilatation term is *extremely difficult to model* and not much success has been achieved in dealing with it. Fortunately, there exist many turbulent flows where the precise details of its structure, as documented in the turbulence literature, are not important. Consequently, at this stage in the development of compressible large-eddy simulations, we propose to defilter \tilde{T} and $\nabla \cdot \tilde{\mathbf{v}}$ and to calculate (46) directly. Since the large scales (which contain most of the turbulent energy) are likely to be the main contributor to the pressure dilatation term, this technique should be relatively satisfactory despite the fact that high frequency information is lost by defiltering. In an analogous manner, the viscous terms on the right-hand side of (16) and (35) can be obtained by defiltering in turbulent flows where the Reynolds numbers are not extremely high or where the turbulence is not in close proximity to solid boundaries.

The turbulence model proposed herein is complete once values for the constants C_R , C_I and C_T are obtained. This will be accomplished using the results of direct numerical simulations of compressible isotropic turbulence.

3. Numerical Method

Our direct simulations of compressible turbulence are based on Eqs. (1)-(3), with the time derivative in the energy equation written solely in terms of the pressure. In order to alleviate the severe stability limit imposed at very low Mach numbers by the acoustic waves, a splitting method is adopted. The first step integrates the equations

$$\frac{\partial \rho}{\partial t} = 0, \quad (47)$$

$$\frac{\partial(\rho v_k)}{\partial t} + \frac{\partial(\rho v_k v_l)}{\partial x_l} = \frac{\partial \sigma_{kl}}{\partial x_l}, \quad (48)$$

$$\frac{\partial p}{\partial t} + v_k \frac{\partial p}{\partial x_k} + \gamma p \frac{\partial v_k}{\partial x_k} - c_0^2 \frac{\partial(\rho v_k)}{\partial x_k} = \frac{1}{RePrM_\infty^2} \frac{\partial}{\partial x_k} \left(\frac{\kappa}{\kappa_0} \frac{\partial T}{\partial x_k} \right) + (\gamma - 1)\Phi, \quad (49)$$

while the second step integrates

$$\frac{\partial \rho}{\partial t} + \frac{\partial(\rho v_k)}{\partial x_k} = 0, \quad (50)$$

$$\frac{\partial(\rho v_k)}{\partial t} + \frac{\partial p}{\partial x_k} = 0, \quad (51)$$

$$\frac{\partial p}{\partial t} + c_0^2 \frac{\partial(\rho v_k)}{\partial x_k} = 0. \quad (52)$$

The constants c_0 and M_∞ are the current root mean square (rms) value of the sound speed and the free-stream Mach number, while $\gamma = C_p/C_v$, where C_v is the specific heat

at constant volume. The free-stream Mach number is M_∞ . These equations are non-dimensionalized in terms of a length scale (l_0), a velocity scale (u_0), and a pressure scale (p_0), a reference viscosity μ_0 and a reference conductivity κ_0 . The Reynolds number is given by $Re = \rho_0 u_0 l_0 / \mu_0$ and the Prandtl number is $Pr = C_p \mu_0 / \kappa_0$. Except for the substitution of $\frac{\mu}{\mu_0}$ for μ , the dissipation function Φ is given by Eq. (5). Initially, the density ρ_0 is uniform and equal to one. Both the viscosity μ and the conductivity κ are constant in this initial study. The computational domain is a cube, normalized to $[0, 2\pi]^3$. Periodic boundary conditions are imposed in all three directions.

The spatial derivatives in these equations are approximated by a Fourier collocation method (see, for example, Hussaini and Zang (1987)). In each coordinate direction, N grid points are used: $x_{k,j} = 2\pi j/N$, for $j = 0, 1, \dots, N-1$. The derivative of a function $\mathcal{F}(\mathbf{x})$ with respect to x_k is approximated by the analytic derivative of the trigonometric interpolant of $\mathcal{F}(\mathbf{x})$ in the direction x_k . Most simulations of incompressible, homogeneous turbulence have used a Fourier Galerkin method. The compressible equations, however, contain cubic rather than quadratic nonlinearities and true Galerkin methods are relatively more expensive (compared with collocation methods) than they are for incompressible flow. The essential difference between collocation and Galerkin methods is that the former are subject to both truncation and aliasing errors, whereas the latter have only truncation errors. As discussed extensively by Canuto, et al (1987), the aliasing terms are not significant for a well-resolved flow. However, care is needed to pose a collocation method in a form which ensures numerical stability. For this reason, the second term in (48) is actually used in the equivalent form $\frac{1}{2}[\frac{\partial(\rho v_k v_l)}{\partial x_l} + \rho v_l \frac{\partial v_k}{\partial x_l} + v_k \frac{\partial(\rho v_l)}{\partial x_l}]$. As noted by Feiereisen, Reynolds and Ferziger (1981), when this form is employed together with a symmetric differencing method in space (for example Fourier collocation), then in addition to mass, and momentum, energy is conserved for the ideal compressible equations (zero viscosity and conductivity) in the absence of time differencing (and splitting) errors.

The second fractional step of the splitting, given by (50) - (52) contains most of the effects of the acoustic waves. This splitting is employed at each stage of a third-order Runge-Kutta method. In the simulations reported here, the second fractional step is integrated analytically. In Fourier space (50)-(52) become

$$\frac{\partial \hat{p}}{\partial t} + i k_l \hat{m}_l = 0 \quad (53)$$

$$\frac{\partial \hat{m}_l}{\partial t} + i k_l \hat{p} = 0 \quad (54)$$

$$\frac{\partial \hat{p}}{\partial t} + i c_0^2 k_l \hat{m}_l = 0 \quad (55)$$

where $m_l = \rho v_l$ and Fourier transformed quantities, which depend upon the wavenumber \mathbf{k} , are denoted by a circumflex. The exact solution of these equations may be written

$$\hat{p}^{(2)} = \hat{p}^{(1)} + \frac{1}{c_0^2} [\hat{A} \cos(c_0 k \Delta t_s) + \hat{B} \sin(c_0 k \Delta t_s) - \hat{A}] \quad (56)$$

$$\hat{m}_i^{(2)} = \hat{m}_i^{(1)} - \frac{ik_i}{c_0 k} [\hat{A} \sin(c_0 k \Delta t_s) - \hat{B} \cos(c_0 k \Delta t_s) + \hat{B}] \quad (57)$$

$$\hat{p}^{(2)} = \hat{A} \cos(c_0 k \Delta t_s) + \hat{B} \sin(c_0 k \Delta t_s) \quad (58)$$

where $k = |\mathbf{k}|$ is the magnitude of the Fourier wavenumber, $\hat{A} = \hat{p}^{(1)}$, $\hat{B} = i \frac{c_0}{k} k_i \hat{m}_i^{(1)}$. The superscript 1 denotes the result of the first fractional step of the splitting and the superscript 2 the results of the second fractional step. The effective time-step of the Runge-Kutta stage is denoted by Δt_s . The advantage of this splitting is that the principal terms responsible for the acoustic waves have been isolated. Since they are treated semi-implicitly, one expects the time-step limitation to depend upon $v + |c - c_0|$ rather than $v + c$. (Although there is also a viscous stability limit for the first fractional step, it is well below the advection limit in the cases of interest.) This is clearly a substantial advantage at low Mach numbers. Since the second fractional step is integrated analytically, it does not contribute to any time step limitations. If one is truly interested in all the details arising from the sound waves, then the time-step must be small enough to resolve the temporal evolution of these waves. But, if only the larger-scale sound waves are of interest, then this splitting method is useful.

During the acoustic fractional step an isotropic truncation is performed: for each variable — ρ , ρv and p , all Fourier coefficients for which

$$k_i k_i \geq (N/2)^2 \quad (59)$$

are set to zero. This reduces the numerical anisotropy produced by a cubic truncation. Moreover, it reduces the aliasing interactions in the collocation method (Canuto et al 1987, Chapters 3 and 7).

The compressible code can also be executed in a purely explicit mode. In this case no splitting is performed; Eqns. (47)-(52) are simply combined in the appropriate manner and integrated directly.

The expected stability limit of this three-dimensional Fourier collocation method for the compressible Navier-Stokes equations has the form

$$\Delta t < \alpha \frac{\Delta x}{u} \quad (60)$$

where for the semi-implicit version u is the maximum value, for any velocity component, of $|v_k| + |c - c_0|$ and, for the explicit version, u is the corresponding maximum of $|v_k| + |c|$. For the third-order Runge-Kutta method employed here the coefficient α should be approximately 1. In practice we have found the explicit code to be stable provided (60) is satisfied with $\alpha = 1.5$ with isotropic truncation. The corresponding limit for the semi-implicit code is roughly 0.4.

A number of simulations have also been conducted of strictly incompressible flow. These were performed with a separate code which also used a Fourier collocation method, but for the simpler, incompressible Navier-Stokes equations.

4. Comparison with Incompressible Results

The initial conditions for the numerical simulations were designed to mimic the experimental data of Comte Bellot and Corrsin (1971), hereafter referred to as CBC. These experiments were also the basis of direct simulations used by Clark, Ferziger and Reynolds (1979), Bardina, Ferziger and Reynolds (1983), and McMillan and Ferziger (1979) in their analyses of LES models for incompressible turbulence. Initial conditions are chosen to match CBC measurements at a non-dimensional time of 240 (cf. table 4 in Comte Bellot and Corrsin 1971). The computational domain is a cube of side 20cm. These parameters are associated with measurements taken behind a grid with a mesh spacing of one inch, and a mean fluid velocity of 393.7 inches/sec. The initial time in the direct simulation corresponds to $t = 0.00254\text{sec}$ in the CBC experiment. The reference length (l_0), velocity (U_0) and pressure (p_0) are respectively $20\text{cm}/2\pi$, $1\text{cm}/\text{sec}$ and $1\text{gr}/\text{cm sec}^2$. After generating a random, divergence-free velocity profile, the kinetic energy (in Fourier space) is scaled to match the measured CBC energy spectrum (see Appendix). Finally, the velocities are scaled so that the initial rms velocity agrees with the measured values. This adjustment is typically less than 1%, which provides one measure of the uncertainty in the fit to the experimental data. With the chosen non-dimensionalization, the Reynolds number $Re = U_0 l_0 / \nu_0$ is 22.74 based on a reference kinematic viscosity $\nu_0 = 0.14 \text{ cm}^2/\text{sec}$. In table 1, the parameters measured by CBC at $t=240$ are summarized. The Taylor microscale

	CBC	64 ³	96 ³	128 ³
σ_u	6.75	6.75	6.75	6.75
$\frac{1}{3}tr(\mathbf{S}\mathbf{k})$	—	0.0	0.0	0.0
E	—	68.3	68.3	68.3
ϵ	462	375	432	447
λ_{11}	0.26	0.28	0.27	0.25
λ_{12}	—	0.20	0.19	0.27
λ_{13}	—	0.20	0.19	0.26
R_λ	38.1	43.6	41.3	37.8

Table 1: Initial conditions based on CBC experiment and Clark et al. (1979) calculation. Mach number is zero.

length λ_{kl} is defined by

$$\lambda_{kl} = \left[\frac{\langle v_k^2 \rangle}{\langle (\frac{\partial v_k}{\partial x_l})^2 \rangle} \right]^{1/2} \quad (61)$$

and the dissipation ϵ by

$$\epsilon = 2\mu \int S_{ij} S_{ij} d^3x, \quad (62)$$

where S_{ij} is the rate of strain tensor

$$S_{ij} = \frac{1}{2} \left(\frac{\partial v_i}{\partial x_j} + \frac{\partial v_j}{\partial x_i} \right). \quad (63)$$

In Eq. (61), $\langle \rangle$ denote a root mean square. Its exact definition is given in the Appendix. The Taylor microscale Reynolds number is

$$R_\lambda = \frac{v_1 \lambda_{11}}{\nu}. \quad (64)$$

The velocity derivative skewness and flatness tensors **Sk** and **Fl** are the third and fourth moments of the velocity gradient and are defined by

$$Sk_{kl} = \frac{\langle \left(\frac{\partial v_k}{\partial x_l} \right)^3 \rangle}{\langle \left(\frac{\partial v_k}{\partial x_l} \right)^2 \rangle^{3/2}} \quad (65)$$

$$Fl_{kl} = \frac{\langle \left(\frac{\partial v_k}{\partial x_l} \right)^4 \rangle}{\langle \left(\frac{\partial v_k}{\partial x_l} \right)^2 \rangle^2}. \quad (66)$$

In tables 1 and 2, only the average diagonal components of the skewness and flatness tensors are shown. The remaining columns list the parameters obtained from the initial conditions of the numerical simulations on 64^3 , 96^3 and 128^3 grids. There is a 20% discrepancy between the dissipation obtained by CBC and the dissipation computed on the coarsest grid which suggests that a 64^3 grid has marginal resolution, at best. A 12% difference between the value of R_λ calculated on the 64^3 grid and that obtained by CBC confirms the need for grids finer than 64^3 . On a 96^3 grid, both the dissipation and R_λ are in much closer agreement with CBC. Discrepancies between our results and CBC for ϵ and R_λ are respectively 6.5% and 7.5% on a 96^3 grid. On the finest grids that the direct simulations were performed on, the computed values of ϵ and R_λ respectively have relative errors of 3.5% and less than 1% when compared to CBC.

The numerical simulations were run from time $t = 240$ until $t = 375$ (in CBC units), which corresponds to a non-dimensional interval of 0.1145 (in our units). Table 2 furnishes a comparison of the experimentally measured parameters with those from the numerical simulation at the final time. On the coarsest grid, the total dissipation rate that was calculated is still slightly below the value measured by CBC. A 96^3 grid generates values of ϵ consistent with CBC.

Skewness measures the departure from symmetry. At $t=0.1145$, the diagonal components of **Sk** are -0.5 which agree well with the numerical results of Kerr (1985). Kerr

	CBC	64 ³	96 ³	128 ³
σ_u	5.03	5.18	5.19	5.21
$\frac{1}{3}tr(Sk)$	—	-0.42	-0.51	-0.52
E	38.6	40.3	40.4	40.7
ϵ	154.4	151.3	154.6	156.8
λ_{11}	0.34	0.33	0.34	0.33
λ_{12}	—	0.24	0.24	0.23
λ_{13}	—	0.24	0.24	0.23
R_λ	36.6	37.8	40.4	37.2

Table 2: Final conditions ($t=0.1145$) based on CBC experiment and Clark et al. (1979) calculation. Mach number is zero.

studied isotropic, turbulent flow, but prevented the decay of energy by using an exterior energy source at the large length scales.

As noted in the previous section, we have chosen not to de-alias the advection terms. In reaching this decision we drew upon the extensive evidence that has accumulated on aliasing effects in the last dozen years (Canuto, et al 1987., Chapters 3, 4 and 7) as well as some tests conducted with the incompressible isotropic turbulence code. In this code, de-aliasing is accomplished by applying the 2/3-rule (Canuto, et al 1987, Chapters 3 and 7) in an isotropic fashion; e.g., the de-aliased results for a 64³ grid are obtained by running the incompressible code on a 96³ grid and applying the truncation given by (59) with 32 in place of $N/2$ on the right hand side. The results are summarized in Fig. 1. Here we present, for 64³, 96³, and 128³ grids, the energy spectra $E(k)$ (defined in the Appendix) at $t = 0.0586$ for both aliased and de-aliased calculations. Some adverse effects of aliasing are apparent on the 64³ grid, but they are only in the tail of the spectra, and they are already insignificant on a 96³ grid. For the reasons outlined here, a 96³ grid was chosen as the standard discretization for the incompressible as well as the compressible simulations.

5. Compressible Turbulence Results

5.1. Direct Simulations

For the compressible case, the initial conditions imposed on the velocity distribution remain unchanged. Reynolds and microscale Reynolds numbers retain the values used in the incompressible simulations. The initial pressure distribution over the entire field is

specified. The fluctuating pressure, p_f is determined from the velocity distribution by enforcing a zero initial time derivative for $\nabla \cdot \mathbf{v}$. A Poisson equation for p_f is obtained from the divergence of the momentum equation after setting the time variation of $\nabla \cdot \mathbf{v}$ to zero (Feiereisen et al. 1981). The mean pressure, p_m , is then determined so that a prescribed initial mean average Mach number, M_0 , defined to be the ratio of rms fluid velocity and rms of the speed of sound, is achieved. An analytic expression for p_m is given by

$$p_m = \frac{M_0^2 \int v^2 d^3\mathbf{x} + \int \frac{\gamma p_f}{\rho} d^3\mathbf{x}}{\gamma \int \rho^{-1} d^3\mathbf{x}}. \quad (67)$$

The initial average Mach number is specified at the outset of the direct simulations (DS) as an initial condition. Density is initially set to unity, while the temperature, if required, is derived from the equation of state.

The Mach 0.6 case contains localized regions of supersonic flow as evidenced by tables 3-5 and by the three-dimensional contour of Mach 1 furnished in figure 2. Nonetheless, the statistical properties of the flow remain largely unaffected by compressibility effects if the average Mach number is in the low subsonic range. This is shown in figures 3-6 which track the time histories of a small number of statistical variables obtained from 96^3 DS. The time histories for skewness (fig. 3), λ (fig. 4), and total kinetic energy (fig. 5) at Mach numbers 0.0, 0.1, 0.4 and 0.6 are virtually superimposed on each other.

Flatness and skewness are affected the most by compressibility effects. Figure 3 indicates that the skewness which corresponds to an isotropic turbulent state monotonically increases with Mach number. It is -0.50 at $M=0$ and has increased to -0.46 at $M=0.6$. Before the flow has reached a state of isotropic turbulence, the time evolution of skewness at all Mach numbers are indistinguishable from each other. The physical system has equilibrated after approximately one third the total computation time. While not reaching an equilibrium value, it is nonetheless worthwhile to point out that the flatness parameter decreases by 2% as the Mach number is raised from 0.0 to 0.6 as seen in figure 6.

Figure 5 illustrates the decay of turbulent kinetic energy ($1/2 u_i u_i$) as a function of time. This decay is a natural consequence of viscous damping. After a brief initial increase, R_λ continuously decreases in time, (as illustrated in figure 7), with no sign of stabilizing. On the other hand, λ which is representative of the medium-scaled eddies, increases in time. This indicates that energy in the higher wavenumbers is being depleted by the molecular viscosity.

Tables 3 to 5 summarize the results of direct simulations of compressible isotropic turbulence at Mach 0.1, 0.4 and 0.6 at $t=0.1145$ on three different grids. Incompressible results are included for comparison. On all the grids, the compressible data converges to the incompressible results as the Mach number is driven towards zero. As expected, the divergence of velocity no longer vanishes, and is now an increasing function of M_0 .

While the dissipation is approximately the same on the two finer grids, the consistently lower values on the coarsest grid confirm the previously stated conclusion that a 64^3 grid

M_0	E	ϵ	$\langle \nabla \cdot \mathbf{v} \rangle$	$\langle \frac{1}{3}tr(\mathbf{Sk}) \rangle$	$\langle M \rangle$	M_{max}
0.0	40.26	157.4	0.00	-0.424	0.00	0.00
0.1	40.82	158.2	0.17	-0.440	0.07	0.21
0.4	41.09	160.4	1.50	-0.428	0.28	0.84
0.6	41.32	162.3	3.30	-0.406	0.43	1.26

Table 3: Summary of direct simulations on a 64^3 grid with initial average Mach numbers of 0.0, 0.1 and 0.4 at $t=0.1145$.

M_0	E	ϵ	$\langle \nabla \cdot \mathbf{v} \rangle$	$\langle \frac{1}{3}tr(\mathbf{Sk}) \rangle$	$\langle M \rangle$	M_{max}
0.0	40.35	154.3	0.00	-0.506	0.00	0.00
0.1	40.49	155.5	0.14	-0.505	0.07	0.23
0.4	40.79	157.0	1.17	-0.493	0.28	0.93
0.6	41.04	158.3	2.82	-0.477	0.42	1.39

Table 4: Summary of direct simulations on a 96^3 grid with initial average Mach numbers of 0.0, 0.1, 0.4 and 0.6 at $t=0.1145$

cannot resolve all the length scales. As a function of increasing Mach number, the trace of \mathbf{Sk} increases, the dissipation decreases, while the total kinetic energy increases very slightly.

The results in tables 3-5 are averages over several DS runs with different initial seeds. A given seed uniquely determines the initial velocity distribution, and therefore the pressure and temperature fields. Variations of the seed are only necessary to eliminate the statistical uncertainty due to the random velocity distribution. The distribution of velocity on two different grid sizes are different even when the initial seed is the same.

Skewness is even more sensitive to the grid refinement than the dissipation as witnessed by its decrease from a value of -0.505 to one of -0.521 on 96^3 and 128^3 grids respectively. This sensitivity might be the result of the derivative of the fluctuating velocity field which appears in the definition of the skewness tensor \mathbf{Sk} .

M_0	E	ϵ	$\langle \nabla \cdot \mathbf{v} \rangle$	$\langle \frac{1}{3}tr(\mathbf{S}\mathbf{k}) \rangle$	$\langle M \rangle$	M_{max}
0.0	40.29	153.98	0.00	-0.521	0.00	0.00
0.1	40.39	154.84	0.14	-0.518	0.07	0.21
0.4	40.78	156.54	1.11	-0.505	0.28	0.86

Table 5: Summary of direct simulations on a 128^3 grid with initial average Mach numbers of 0.0, 0.1 and 0.6 at $t=0.1145$

5.2. Data Analysis

Using the data generated from the previously discussed DS of compressible homogeneous turbulence at low Mach numbers, the proposed subgrid-scale (SGS) model is validated. If a good model is to be successful, it must require that the subgrid stresses calculated from the DS correlate well with the computed model stresses. Models express the subgrid scale stresses, not available to a large eddy simulation code, as a function of the large eddy velocities which are known. These velocities are simply the Favre-filtered velocities introduced earlier. The Favre-filtered velocities are calculated by filtering the resolved DS velocity field with a Gaussian spatial filter of width $\Delta_f \Delta x_f$, where Δx_f is the grid spacing on the fine grid. Perturbed velocity fluctuations on the fine grid are the difference between the fully resolved velocity and the filtered ones,

$$\mathbf{v}' = \mathbf{v} - \tilde{\mathbf{v}}. \quad (68)$$

From \mathbf{v}' and $\tilde{\mathbf{v}}$ subgrid stresses based on DS, considered exact, are calculated. These include the Leonard (21), cross (22) and Reynolds (23) subgrid stresses. However, these subgrid-scale stresses themselves do not directly affect the evolution of the system. The momentum equation is only influenced by the divergence of the subgrid stresses (vector level). Similarly, $\tilde{\mathbf{v}} \cdot \nabla \cdot \boldsymbol{\tau}$ (scalar level) is a better representation of the dissipation terms in the energy equation than are the stresses. Consequently, correlations are performed on the tensor, vector and scalar levels. High correlations must be achieved on all levels of comparisons before the SGS model can be considered useful.

The data analysis proceeds in multiple stages. First, the exact stresses calculated from the DS are injected down to the coarse grid, along with with the filtered velocities. The modeled subgrid stresses are then calculated (excluding the model constants) on the coarse grid. Some variables must be filtered a second time (e.g. cross stress terms). Rather than calculate them on the fine grid (which is not available to the large-eddy simulation codes), a Gaussian filter is applied to $\tilde{\mathbf{v}}$ on the coarse grid with a filter width of $\Delta_c \Delta x_c$. Consistency

between the coarse and fine filter widths is achieved by insuring that

$$\frac{\Delta_f}{\Delta_c} = \frac{N_f}{N_c} \quad (69)$$

where N_f and N_c are respectively the number of nodes along one direction on the fine and coarse grids. This guarantees that the filtering on the coarse and fine grid is performed over the same region in physical space. Henceforth, the coarse and fine filter widths are referred to in their non dimensional form Δ_c and Δ_f . Derivative evaluations on both the coarse and the fine grid are based on Fourier collocation. Calculations by McMillan and Ferziger (1979) indicate that the model constants are sensitive to the accuracy of the derivative evaluations. A general trend that has been observed is that the Smagorinsky constant is lowered when derivative quantities are evaluated more accurately. Our constants are therefore expected to lie in the lower range of the values obtained by McMillan (1980).

Next, the two model constants, C_R and C_I , are calculated. Unfortunately, the constants can be calculated by a wide variety of algorithms, each with its own merits. Moreover, for each algorithm, the constants can be evaluated from tensor, vector or scalar information. Therefore, criteria must be established to identify the best method. A key test is that $\mathbf{L} + \mathbf{R}$ should be Galilean invariant. To make use of this fact, an additional constant, C_C , is introduced as an extra factor in the subgrid cross stress model. A self consistent method of calculating the constants will have to produce a C_C of 1 to satisfy the Galilean invariance property stated above (Speziale 1985). Additional tests are performed on coarse grids with varying degrees of refinement which further decrease the number of choices. A thorough discussion of model constants is the subject of the next subsection.

Once a single or a multiple set of model constants have been determined, the model subgrid stresses are calculated and correlated with the exact subgrid-scale stresses calculated from the DS after injection onto the coarse grid. The correlations are performed for each type of subgrid-scale stress individually, and for the total stress ($\mathbf{L} + \mathbf{C} + \mathbf{D}\mathbf{R} + \mathbf{I}\mathbf{R}$). Strong differences in the correlation coefficients relating total stresses are noticed depending on whether or not the Leonard stresses are included. Finally, the correlations obtained from the proposed model are compared with the linear combination model, which has been shown to be the best model available for incompressible isotropic turbulence. Correlation coefficients are calculated based on the two pairs of constants that are obtained from the above considerations. The set that is finally retained corresponds to the highest levels of correlation of the total stress on the vector and scalar levels. These matters are treated more completely in a later subsection.

To avoid a possible confusion of terminology when referring to variables being compared against each other, superscripts $()^m$ and $()^e$ are sometimes used. They respectively refer to modeled and exact (based on DS) variables (tensor, vector or scalar level).

5.2.1. Model Constants

The proposed model (32) has two undetermined coefficients. The first constant, C_R , is associated with the modeled deviatoric subgrid Reynolds stress, $_D\mathbf{R}$, while the second constant, C_I , allows the modeled isotropic stress, $_I\mathbf{R}$ to be adjusted.

Although the cross stress model has no constant associated with it, it is nonetheless multiplied by a constant C_C . This is done in the hope of reducing the number of schemes by which the constants can be calculated. A good model should reproduce a cross constant of one to guarantee the Galilean invariance of \mathbf{C}^m . Once the constants have been determined, C_C is set to one and forgotten. Because the flow is isotropic, constants are expected to be the same for the three diagonal stress components, the three off-diagonal components and the three vector components. Therefore, the values presented in the tables below are averaged over the appropriate components. In the tables, D refers to averaged diagonal components, OD to average off-diagonal components, V to averaged vector components and S to scalar components. Similar averagings are performed for correlation coefficients.

The three constant models (C_R , C_I and C_C) are calculated using two techniques, each applied on the tensor, vector and scalar levels. One method enforces equality of the rms levels of the exact and the modeled stress. This is done for each individual subgrid-scale stress (deviatoric and isotropic parts of the subgrid-scale Reynolds stress and the cross stress). Hereafter this approach is referred to as RMS. The second method utilizes multiple linear least square regression (LSQ) between the exact (19) and the modeled (32) total subgrid-scale stress to determine the constants. Table 6 summarizes the results obtained from incompressible data. The three cases presented are identical except for the initial random number seed. The constants are independent of the detailed velocity statistics, except for C_I^{LSQ} which varies randomly. These results are based on a vector level comparison between the modeled and exact stresses. Both RMS and LSQ produce C_C close to unity as required. Unfortunately this prevents a rational choice from being made between the two approaches. A more complete set of LSQ constants is presented in table 7. They are computed at Mach numbers of 0.0, 0.1, 0.4 and 0.6 on a tensor, vector and scalar level. Computations are performed on a coarse grid of 16^3 . Confirming the results of table 6, C_I has strong variations as a function of Mach number on the vector level when the random seed is changed. Additionally, C_I is the subject of random fluctuations at the scalar level. On the tensor level, C_I is quite independent of Mach number and the random seed. A possible interpretation of the variation is that the isotropic stresses do not have much influence on the total stress correlations. That this is indeed the case is explained in the section on correlations. The remaining constants are stable. That is to say, they are very little influenced by either Mach number or initial conditions.

At first glance, C_C is near unity at both the scalar and vector levels. However whereas on the vector level, the constant remains within 4% of unity for all Mach numbers, this is not the case on the scalar level where C_C is a decreasing function of Mach number. This trend is present in the data generated from both random seeds. Although not presented

Seed	LSQ			RMS		
	C_R	C_I	C_C	C_R	C_I	C_C
1	0.012	0.0070	1.04	0.023	0.036	1.03
2	0.012	0.0024	1.03	0.022	0.034	1.04
3	0.012	0.0055	1.03	0.022	0.033	1.03

Table 6: Model constants calculated by LSQ and RMS between exact and modeled total stresses ($\mathbf{L} + \mathbf{C} + \mathbf{R}$). Results are based on three identical incompressible simulations except for the random initial velocity distributions. Calculations are on the vector level on a 16^3 grid.

here, the RMS cross stress model constant is also near unity when calculated based on vector level stresses. Therefore, a preferred method for the determination of the model constants is still not possible.

5.2.2. Filter Width and Grid Coarseness

Confirmation of the numerical evidence presented by McMillan and Ferziger (1979) that $\Delta_c = 2$ is the best filter width is given in table 8 ($M_0 = 0.1$). The criterion used to determine the validity of the filter width is that C_C^{RMS} must remain close to unity on the vector level. Only when $\Delta_c = 2$ is C_C near one. Similar results hold for LSQ constants. The constants also vary with respect to the coarse grid on which the LES is to be performed. Table 9 summarizes the model LSQ and RMS constants evaluated from modeled stresses calculated on 16^3 and 32^3 grids on the vector level. The data ($M_0 = 0.1$) shows that C_R varies by 30% when the grid size on which the modeled stresses are calculated ranges from 16^3 to 32^3 . On the other hand, large eddy simulations using finite difference algorithms might be performed on grids as large as 128^3 . Unless a subgrid scale model is found which produces constants independent of the coarse grid size, LES simulations will run the risk of producing the wrong results. Perhaps a more complicated dependence of the modeled subgrid Reynolds stresses on Δ is required.

The best model constants will produce the highest correlations between the modeled and exact subgrid stresses on all levels (tensor, vector and scalar). Based on the previous discussion, only constants calculated on a vector level are adequate because they produce a C_C of unity. Unfortunately, a clear cut choice between RMS and LSQ constants cannot be made because C_C (on the vector level) is nearly one in both cases. Rather than make an arbitrary choice, both sets of constants are considered when correlating exact against

modeled stresses. For reference, the constants used henceforth are

$$C_R^{LSQ} = 0.012 \quad C_I^{LSQ} = 0.0066 \quad (70)$$

$$C_R^{RMS} = 0.023 \quad C_I^{RMS} = 0.035. \quad (71)$$

		Seed 1				Seed 2	
M_0		0.0	0.1	0.4	0.6	0.0	0.6
C_I	D	0.12	0.12	0.12	0.12	0.11	0.11
	V	—	0.0070	0.0067	0.0063	0.0023	0.0023
	S	—	.0034	.00012	-0.25	.0017	.0003
C_C	D	1.32	1.32	1.32	1.31	1.32	1.31
	V	1.04	1.04	1.02	1.00	1.04	1.00
	S	1.00	1.00	0.95	0.873	0.971	0.934
C_R	D	0.018	0.018	0.018	0.018	0.016	0.015
	V	0.012	0.012	0.012	0.012	0.012	0.012
	S	0.015	0.015	0.015	0.014	0.015	0.015

Table 7: LSQ model constants. Filter widths are $\Delta_f = 12$ and $\Delta_c = 2$

		LSQ			RMS		
Δ_f		6	12	24	6	12	24
Δ_c		1	2	4	1	2	4
C_R		0.007	0.012	0.020	0.019	0.023	0.034
C_I		-0.02	0.002	0.014	0.034	0.030	0.051
C_C		0.31	1.03	1.33	0.82	1.03	1.13

Table 8: LSQ and RMS model coefficients between exact and modeled stresses on the vector level at $M_0 = 0.1$. Results are obtained with fine filter widths of 6, 12 and 24 while maintaining the proper ratio of 6 between fine and coarse widths. The coarse grid is 16^3 .

5.2.3. Correlations

Correlation coefficients have long been a preferred diagnostic tool for estimating the *reliability* of the modeled stresses. However, the subgrid stresses have been separated into

Grid	LSQ			RMS		
	C_R	C_I	C_C	C_R	C_I	C_C
16^3	0.0125	0.0024	1.03	0.023	0.030	1.03
32^3	0.0094	0.0002	1.03	0.013	0.019	1.02

Table 9: LSQ and RMS model constants based on subgrid stresses evaluated on 16^3 and 32^3 coarse grids

various components (\mathbf{L} , \mathbf{C} , \mathbf{R}), each modeled separately and although the correlation of any of these components against their models might be excellent, it is still possible for the correlation of the exact total stress against the modeled total stress to be less impressive. Such is the case, for instance, when two stress components have opposite signs and partially cancel each other out. As a final note before the specific correlation coefficients are presented, one must always be attentive to the actual relationship between the exact and the modeled variable, even when the correlation coefficient is relatively high (say, above 70%). A correlation coefficient as high as 70% may not be as good as it seems. For example, the correlation between the parabola $y = x^2$ and the constant $y = 1$ in the interval $[0, 1]$ is 75% although they are uncorrelated. As a consequence, correlations are deemed good if the correlation coefficient is above, at least the 90% level.

For convenience, the compressible subgrid scale model is restated here:

$$_DR_{ij} = 2C_R \bar{\rho} \Delta^2 (\tilde{S}_{kl} \tilde{S}_{kl})^{1/2} (\tilde{S}_{ij} - \frac{1}{3} \tilde{S}_{mm} \delta_{ij}) \quad (72)$$

$$_IR_{ij} = -\frac{2}{3} C_I \bar{\rho} \Delta^2 (\tilde{S}_{kl} \tilde{S}_{kl}) \delta_{ij} \quad (73)$$

$$C_{ij} = -\bar{\rho} (\tilde{v}_i \tilde{v}_j - \tilde{v}_i \tilde{v}_j) \quad (74)$$

The correlation coefficients presented in table 10 between exact and modeled $_IR$, $_DR$ and \mathbf{C} , are independent of the model constants. The correlation coefficients are insensitive to the average Mach number variation, except for the isotropic stress correlation coefficients which exhibit higher values for the larger Mach numbers. Although the isotropic stresses enjoy a correlation above 80% on the tensor level, the correlation coefficients plummet below 15% on the vector and scalar levels (we will see later that these low correlations are not of great consequence). This indicates that the isotropic modeling is poor.

In most of the literature on subgrid-scale models, the Leonard stress has been omitted from the total stress correlations on the grounds that it is calculated exactly (Bardina, Ferziger, and Reynolds 1983, McMillan 1980, McMillan and Ferziger 1979). However, it has

M_0		0.1	0.4	0.6
${}_D\mathbf{R}$	D	31	31	31
	OD	26	26	25
	V	22	22	22
	S	45	45	45
\mathbf{C}	D	89	89	89
	OD	91	91	91
	V	80	80	80
	S	75	74	72
${}_I\mathbf{R}$	D	84	85	85
	V	13	15	18
	S	12	14	18

Table 10: Correlations between exact and modeled stresses. Shown are the correlations for ${}_D\mathbf{R}$, ${}_I\mathbf{R}$, and \mathbf{C} at Mach 0.1, 0.4 and 0.6.

recently been shown by Speziale (1985) that the combination $\mathbf{L} + \mathbf{C}$ is Galilean invariant, while the cross stress is not. Therefore we feel that correlations of the total stress should include the Leonard stress. Table 11 summarizes the correlation coefficients between the total stress including and excluding the Leonard stress. Results are presented at Mach 0 and Mach 0.6. When the Leonard stresses are left out, correlation coefficients similar to Bardina's are obtained on all levels, even though Bardina did not include the contribution of the isotropic stresses. However, the inclusion of \mathbf{L} decreases the correlations at the vector level by approximately 30%. Table 11 substantiates that the correlation coefficients (with and without \mathbf{L}) are nearly independent of the initial average Mach number.

Correlation coefficients between $(\mathbf{C} + \mathbf{R})^e$ and various combinations of the modeled stresses using constants calculated by LSQ and RMS are summarized in table 12. The second column indicates the model against which the total stress is being compared. Although at first glance RMS based constants perform better at a tensor level when the total modeled stress is considered, at the vector and scalar levels, the trend is reversed. Correlations at the vector and scalar level are higher by 4% using the LSQ constants. The only cases where this trend is absent is when either \mathbf{R} or ${}_I\mathbf{R}$ is removed from the modeled total stress in which case the choice of constants has a negligible effect on the correlation coefficients.

When the constants are selected based on LSQ, table 12 indicates that the correlations on all levels are highest when all modeled components are included. The inclusion of ${}_I\mathbf{R}$ only affects correlations on the tensor level. However, the dynamic evolution of the

	$M_0 = 0.0$		$M_0 = 0.6$	
	L+C+R	C+R	L+C+R	C+R
D	93	82	93	81
OD	80	85	79	84
V	46	72	46	71
S	56	73	56	74

Table 11: Comparison of correlation coefficients of the exact total stress versus its model. The modeled terms are computed on a 16^3 coarse grid. Each case is presented with and without the inclusion of the Leonard subgrid-scale stress terms (calculated exactly). Both the incompressible and the $M=0.6$ case are shown to illustrate the weak influence of Mach number on the correlation coefficients. Model coefficients are $C_R = 0.012$ and $C_I = 0.0066$.

large scale velocities only brings into play the stresses on the vector and scalar level. Therefore the coefficients which produce the maximum correlations of total stress on these two levels should be chosen. This leads to an optimum choice of

$$\begin{aligned} C_R &= 0.012 \\ C_I &= 0.0066 \end{aligned} \tag{75}$$

calculated by least squares fit of the total stress on the vector level.

Conversion of C_R to the standard form currently used in incompressible LES[†] produces a Smagorinsky constant of 0.092. McMillan (1979) obtained a value of $C_S = 0.10$ when spectral collocation derivative computations were employed. This constant corresponds to a scalar level evaluation based on RMS. On the vector level, McMillan calculated a higher Smagorinsky constant of 0.13. This value can be obtained from the present data by using $\mathcal{D}\mathbf{R}^{RMS}$ instead of $\mathcal{D}\mathbf{R}^{LSQ}$. However as shown above, the correlations of the total subgrid stress would be lower.

Yoshizawa (1986) recently performed a direct interaction approximation calculation based on a model for slightly compressible turbulent flows. His model for the isotropic component of the subgrid Reynolds stress is identical to ours. However he calculates $C_I = 0.177$, to be compared to our value of 0.0066[‡]. Yoshizawa also obtains a Smagorinsky

[†]In a number of reports (McMillan and Ferziger 1979, Bardina et al. 1983), the subgrid Reynolds stress model is proportional to C_S^2 . In these cases, the relationship between C_S and C_R is $C_R = \sqrt{2}C_S^2$.

[‡]This comparison must be viewed cautiously since Yoshizawa (1986) did not base his model on Favre-filtered fields

		Least squares				RMS			
		$C_R=0.0122, C_I=0.0066$				$C_R=0.023, C_I=0.035$			
Exact	Model	D	OD	V	S	D	OD	V	S
C+R	C	78	82	68	62	78	82	68	62
	C+ $_I$ R	81	82	69	62	89	82	67	61
	C+ $_D$ R	78	84	71	70	77	83	69	69
	C+R	81	84	71	70	88	83	67	67

Table 12: Correlation of the exact total stress (C+R) with various models. The modeled stresses are defined in equations (72)-(74)

constant $C_S = 0.17$ which is consistent both with incompressible results and the results in this paper.

Results presented in table 12 indicated that the isotropic stresses do not noticeably influence the modeled total stress on the vector and scalar level. When the Navier-Stokes equations are written in the incompressible form, the isotropic stress and the trace of the cross stress can be included with the pressure to form a new total pressure variable. Although this cannot be done for compressible flows because the pressure satisfies an evolution equation of its own, it seems plausible that the isotropic stress should exert very little influence if its rms value is much smaller than the rms of pressure and if the same relation holds true between the gradients of these quantities. At Mach 0.6, the rms value of the pressure and pressure gradient are 283 and 92, respectively, as opposed to the corresponding values of 7.1 and 4.4 for the isotropic Reynolds subgrid-scale stress. These values verify the fact that this term does not play an important role. At lower Mach numbers, the ratio between the rms isotropic stresses and the rms pressure is even greater, and tends to infinity in the incompressible limit. At $M=0$ it is well known that the isotropic stresses have no influence on the velocity distributions.

Total stress correlations obtained with the compressible model are compared with results calculated with the linear combination model and are summarized in table 13. Data is based on the LSQ model constants. The most meaningful comparison is at $M = 0.0$ where the exact, and modeled cross and Reynolds stress are isotropized. The first two lines of the table show a very good agreement between Bardina's results and ours. However, the third line, which includes $_I$ C in the modeled and exact total subgrid stress, generates a correlation coefficient of 70% on the scalar level, or 10% higher than that obtained by Bardina.

Initial tests of the subgrid-scale heat flux model produced a turbulent Prandtl number

	Exact	Model	Stress	Vector	Scalar
Bardina	${}_D\mathbf{C} + {}_D\mathbf{R}$	${}_D\mathbf{C} + {}_D\mathbf{R}$	83	74	60
$M_0 = 0.0$	${}_D\mathbf{C} + {}_D\mathbf{R}$	${}_D\mathbf{C} + {}_D\mathbf{R}$	86	77	60
$M_0 = 0.6$	$\mathbf{C} + {}_D\mathbf{R}$	$\mathbf{C} + {}_D\mathbf{R}$	85	73	71

Table 13: Comparison of the linear combination model (row 1) with two different combinations of subgrid-scale stresses at Mach 0.0 and 0.6 (rows 2 and 3). Correlations were obtained on a coarse grid of 16^3 .

of

$$Pr_T = 0.4 \quad (76)$$

which is a little low compared to the expected value of approximately 0.7. This may be due to the fact that the temperature gradients are not very large in this problem, and hence, these numerical results may not be well suited for the accurate calculation of Pr_T . This issue will be addressed in a future study.

6. Conclusion

New subgrid-scale models for compressible turbulence have been developed and tested against the results of direct numerical simulations of compressible isotropic turbulence. These compressible subgrid-scale models, which were based on the Favre-filtered equations of motion for an ideal gas, contain three dimensionless constants and reduce to the linear combination model in the incompressible limit. The subgrid-scale stress model constants were found to assume the values of $C_R = 0.012$ and $C_I = 0.0066$ and those gave rise to correlations between the exact and modeled stresses that were above 70% on the tensor, vector and scalar levels – a correlation which compares favorably with those obtained in the previous subgrid-scale modeling of incompressible turbulent flows. Another encouraging feature lies in the fact that these constants and their associated correlations were found to be comparatively insensitive to the Mach number in the range $0 < M_0 < 0.6$. While the modeling of the isotropic part of the subgrid-scale Reynolds stress is relatively poor, it appears that it does not play a significant role in the dynamics of the flow for the range of Mach numbers considered in this study. Likewise, the turbulent Prandtl number obtained herein ($Pr_T = 0.4$) appears to be somewhat inaccurate. We believe that this problem can be alleviated by conducting correlations on the basis of turbulence computations which involve more intense temperature gradients (an effort which must await future research).

Future large-eddy simulations of compressible turbulent flows are planned based on the subgrid-scale models developed in this study. Undoubtedly, as such studies progress, additional refinements in these models will be introduced. Nevertheless, we believe that the essential foundations for the large-eddy simulation of compressible turbulent flows have been established in this study. This could have a profound impact on the future analysis of supersonic and hypersonic flows in aerodynamics.

References

- Arfken, G. 1970 *Mathematical Methods for Physicists*. Academic Press.
- Bardina, J., Ferziger, J. H., & Reynolds, W. C. 1983 Improved Subgrid-Scale Models based on Large-Eddy Simulation of Homogeneous, Incompressible, Turbulent Flows. Stanford Report TF-19.
- Batchelor, G. K. 1967 *An Introduction to Fluid Dynamics*. Cambridge University Press.
- Biringen, S. & Reynolds, W. C. 1981 Large-Eddy Simulation of the Shear-Free Turbulent Boundary Layer. *J. Fluid Mech.*, **103**, 53-63.
- Canuto, C., Hussaini, M. Y., Quarteroni, A. & Zang, T. A., 1987 *Spectral Methods in Fluid Dynamics*. Springer-Verlag.
- Clark, R. A., Ferziger, J. H. & Reynolds, W. C. 1979 Evaluation of Subgrid-Scale Models using an Accurately Simulated Turbulent Flow. *J. Fluid Mech.* **91**, 1-16.

- Comte-Bellot, G. & Corrsin, S. 1971 Simple Eulerian Time Correlation of Full and Narrow-Band Velocity Signals in Grid-Generated, Isotropic Turbulence. *J. Fluid Mech.* **48**, 273-337.
- Deardorff, J. W. 1970 A Numerical Study of Three-Dimensional Turbulent Channel Flow at Large Reynolds Numbers *J. Fluid Mech.* **41**, 453-480.
- Eidson, T.M. 1985 Numerical Simulation of Turbulent Rayleigh-Benard Problem using Numerical Subgrid Modeling. *J. Fluid Mech.* **158**, 245-268.
- Feiereisen, W. J., Reynolds, W. C. & Ferziger, J. H. 1981 Numerical Simulation of Compressible, Homogeneous, Turbulent Shear Flow. Report TF-13, Dept. Mech. Eng., Stanford University.
- Hinze, J. O. 1975 *Turbulence*. McGraw-Hill.
- Hussaini, M. Y., & Zang, T. A. 1987 Spectral Methods in Fluid Dynamics. *Ann. Rev. Fluid Mech.* **19**, 339-368.
- Kerr, R. M. 1985 Higher-Order Derivative Correlations and the Alignment of Small-Scale Structures in Isotropic, Numerical Turbulence. *J. Fluid Mech.* **153**, 31-58.
- Leonard, A., 1974 On the Energy Cascade in Large-Eddy Simulations of Turbulent Fluid Flows. *Adv. Geophys.* **18**, 237-248.
- Lumley, J. L. 1983 Turbulence Modeling. *ASME J. Appl. Mech.* **50**, 1097-1103.
- McMillan, O. J. 1980 Tests of New Subgrid-Scale Models in Strained Turbulence. AIAA paper AIAA-80-1339, in *AIAA 13th Fluid and Plasma Dynamics Conference*, Snowmass, Co.
- McMillan, O. J. & Ferziger, J. H. 1979 Direct Testing of Subgrid-Scale Models. *AIAA J.* **17**, 1340-1346.
- Reynolds, W. C. 1976 Computation of Turbulent Flows, *Ann. Rev. Fluid Mech.* **8**, 183-208.
- Rogallo, R. S. & Moin, P. 1984 Numerical Simulation of Turbulent Flows. *Ann. Rev. Fluid Mech.* **16**, 99-137.
- Schumann, U. 1975 Subgrid Scale Model for Finite Difference Simulations of Turbulent Flows in Plane Channels and Annuli. *J. Comput. Phys.* **18**, 376-404.
- Speziale, C. G. 1985 Galilean Invariance of Subgrid-Scale Stress Models in the Large-Eddy Simulation of Turbulence. *J. Fluid Mech.* **156**, 52-62.
- Tennekes, H. & Lumley, J. L. 1972 *A First Course in Turbulence* MIT press.

Voke, P. R. & Collins, M. W. 1983 Large-Eddy Simulation: Retrospect and Prospect. *PhysicoChemical Hydrodynamics* 4, No. 2, 119-161.

Yoshizawa, A. 1986 Statistical Theory for Compressible Turbulent Shear Flows, with the Application to Subgrid Modeling, *Phys. Fluids* 29, 2152-2164.

Appendix

Initial energy spectrum

Both the incompressible and compressible direct simulations impose a specified energy spectrum on the initial random velocity distribution. For comparative purposes, the data was obtained from tabular data found in Comte-Bellot and Corrsin (1971). They tabulate the function $E_{11}(k)$ which is related to the energy spectrum $E(k)$ by

$$E(k) = \frac{1}{2}k^3 \frac{d}{dk} \left[\frac{1}{k} \frac{dE_{11}}{dk} \right]. \quad (A1)$$

Unfortunately the data is noisy, so a least squares fit is performed on $\log E_{11}$, expressed as a fourth order polynomial in $\log k$. The final form obtained for E_{11} is

$$\begin{aligned} \log(E_{11}) = & 2.64359 - 0.72602(\log k) - 0.32585(\log k)^2 \\ & + 0.03525(\log k)^3 - 0.02344(\log k)^4. \end{aligned} \quad (A2)$$

Calculation of model constants

Before correlating the total exact subgrid stress against its model, the model constants must be determined. There are many ways of accomplishing this among which two are retained. The total modeled stress is written as a linear combination of modeled terms $C_i \tau_i^m$:

$$\tau^m = \sum_{i=1}^n C_i \tau_i^m \quad (A3)$$

while the exact total stress is simply

$$\tau^e = \sum_{i=1}^n \tau_i^e. \quad (A4)$$

The unknown constants to be determined are the C_i . The first approach adopted is to calculate the root mean square of the pairs $C_i \tau_i^m$ and τ_i^e and equate them for each value of i . The constants thus take the values

$$C_i = \frac{\sigma_{\tau_i^e}}{\sigma_{\tau_i^m}}. \quad (A5)$$

This method is referred to by RMS in the text.

A least square method applied to the total stress as a whole is an alternative approach. In this case, the norm

$$\|\tau^m - \tau^e\|^2 = \left\| \sum_{i=1}^n (\tau_i^e - C_i \tau_i^e) \right\|^2 \quad (\text{A6})$$

is minimized with respect to the coefficients C_i . This gives rise to a linear system in the coefficients which can be solved by direct methods if the number of constants is not too large. For the subgrid model considered in the text, $n = 3$.

Definitions

For reference purposes, several statistical definitions are provided here. All variables are defined on a three-dimension grid and are subscripted by a single index i for convenience. The average of a function \mathcal{F}_i is

$$\langle \mathcal{F} \rangle = \frac{1}{N} \sum_{i=1}^N \mathcal{F}_i. \quad (\text{A7})$$

As a function of the average, the rms of \mathcal{F} is

$$\sigma_{\mathcal{F}} = \sqrt{\langle (\mathcal{F} - \langle \mathcal{F} \rangle)^2 \rangle}. \quad (\text{A8})$$

Correlation coefficients are fundamental in evaluating subgrid-scale models. The correlation coefficient between two functions \mathcal{F} and \mathcal{G} is

$$C(\mathcal{F}, \mathcal{G}) = \frac{\langle \mathcal{F} \mathcal{G} \rangle}{\sigma_{\mathcal{F}} \sigma_{\mathcal{G}}}. \quad (\text{A9})$$

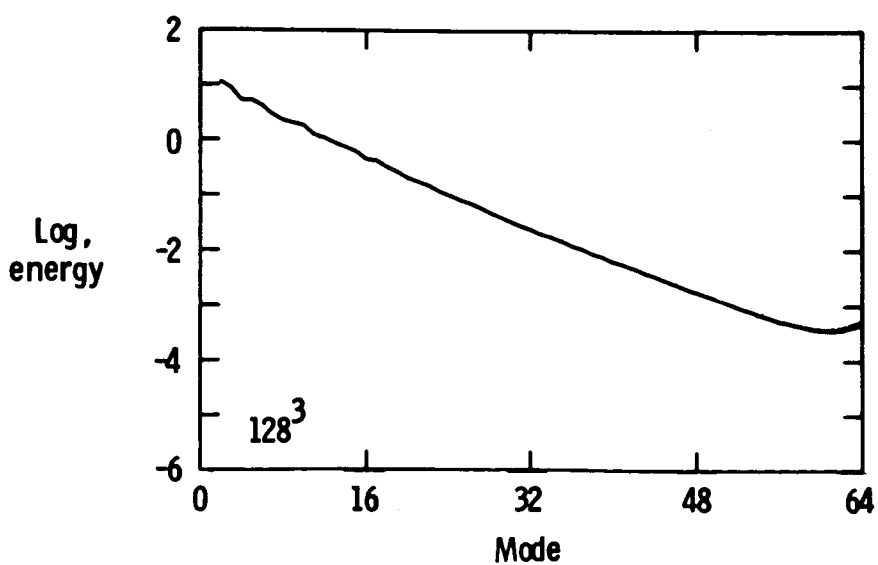
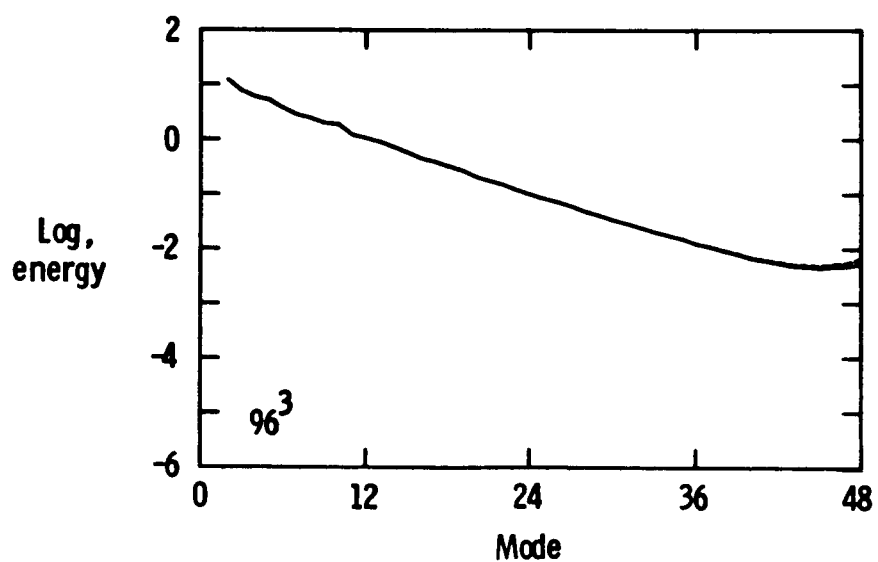
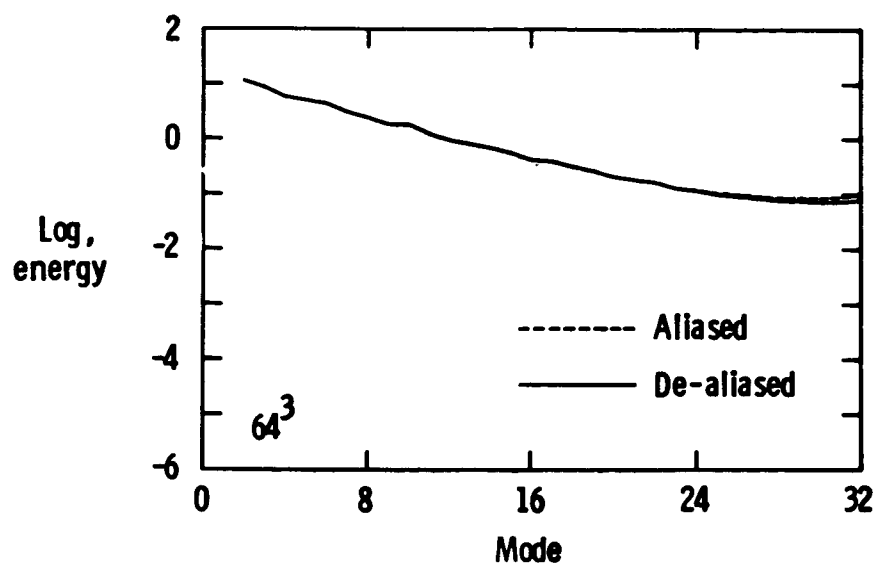


Fig. 1 Energy spectra at $t = 0.0586$ for both aliased and dealiased calculations for 64^3 , 96^3 , and 128^3 grids.

ORIGINAL PAGE IS
OF POOR QUALITY



Fig. 2 Three-dimensional Mach 1.0 contours of a M_0 direct simulation at $t = 0.0586$. The direct simulation was performed on a 96^3 grid.

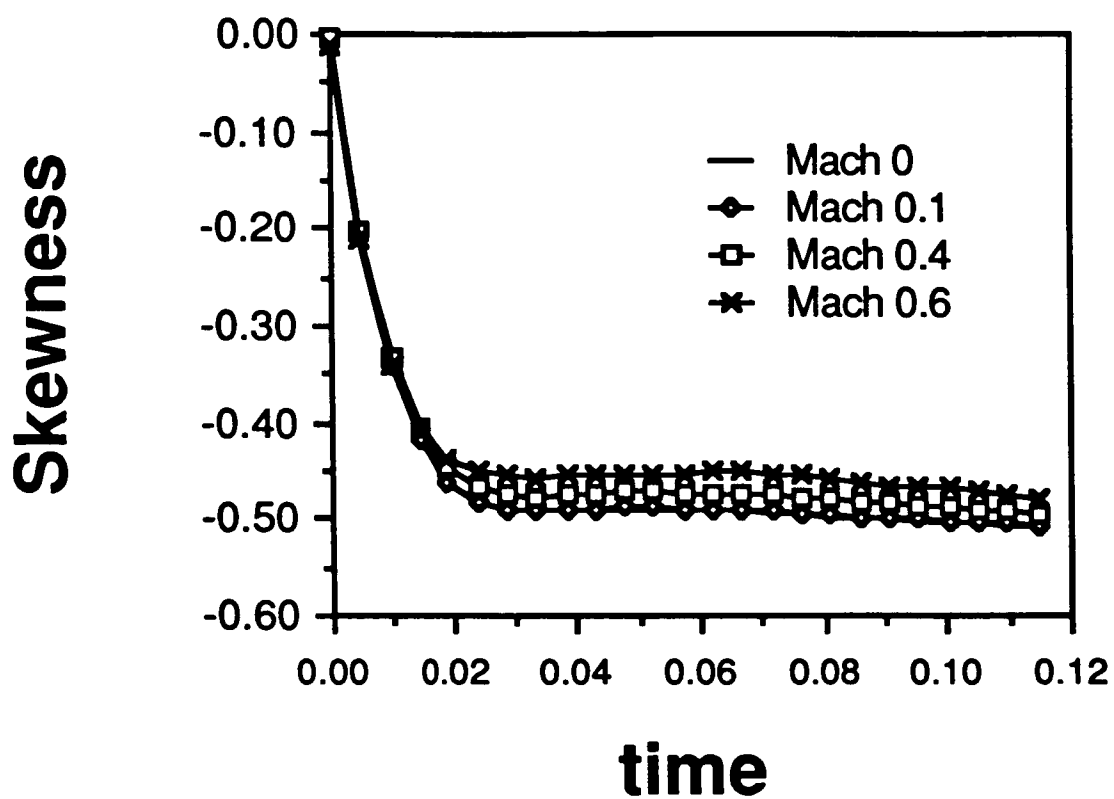


Fig. 3 Time history of one third the trace of S_k for M_0 of 0.0, 0.1, 0.4 and 0.6. Direct simulation was performed on a 96^3 grid.

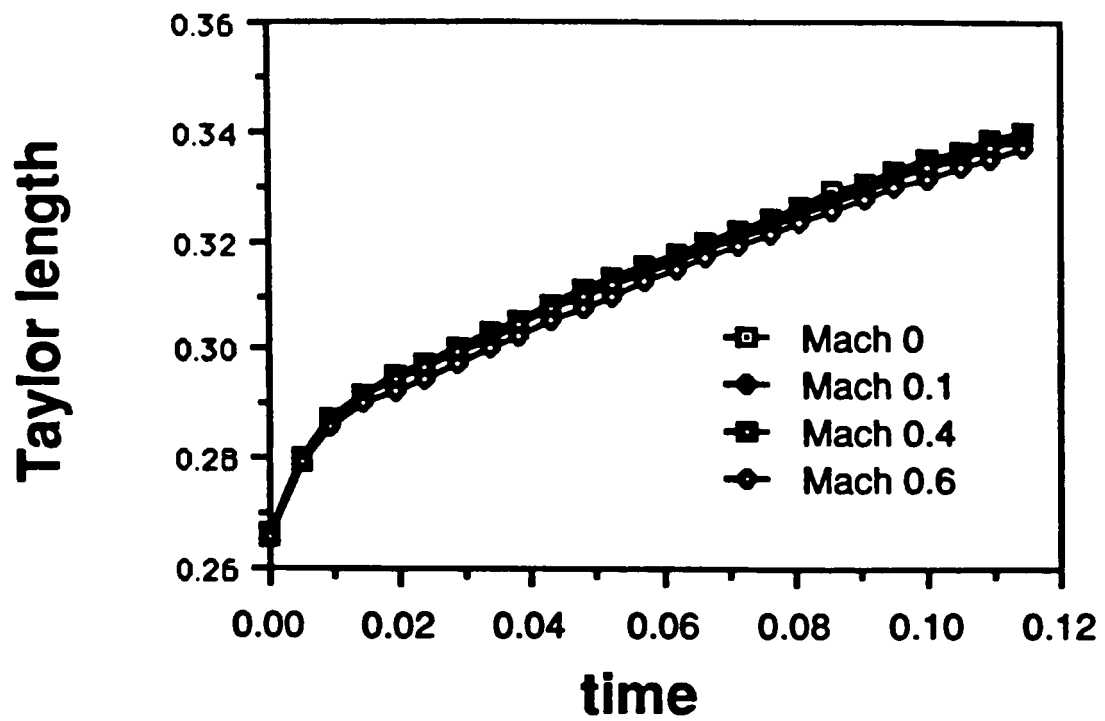


Fig. 4 Time history of one third the trace of λ_{ij} for M_0 of 0.0, 0.1, 0.4 and 0.6. Direct simulation was performed on a 96^3 grid.

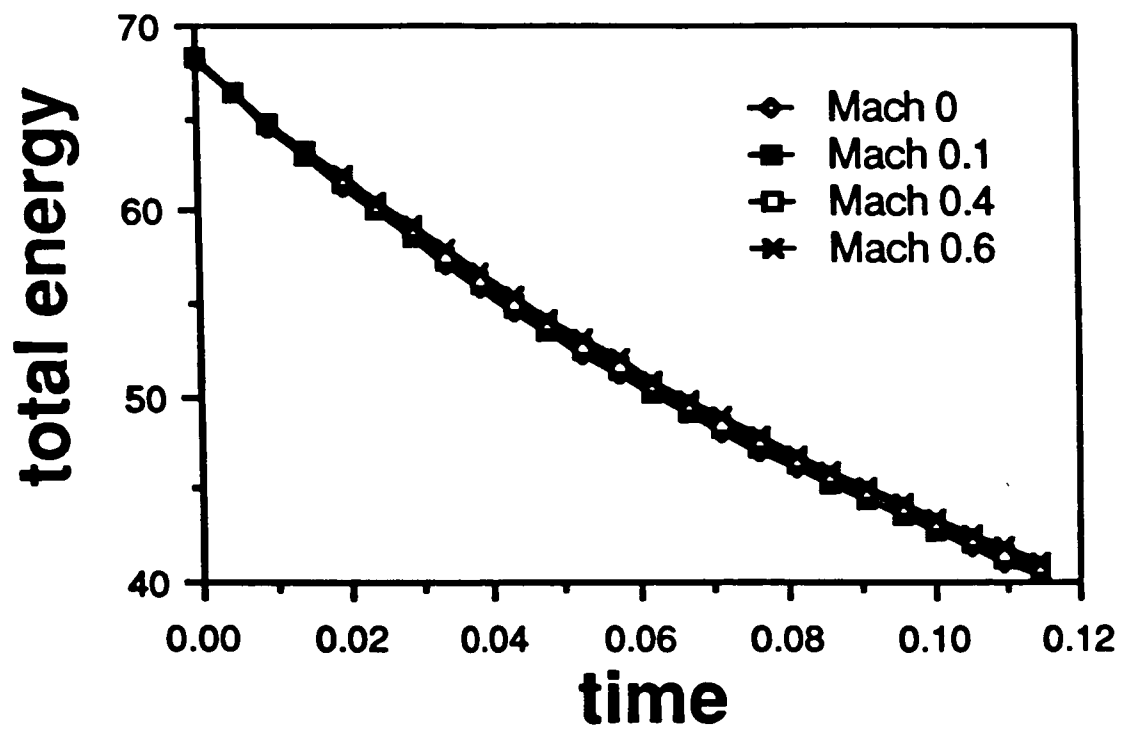


Fig. 5 Time history of one third the trace of kinetic energy for M_0 of 0.0, 0.1, 0.4 and 0.6. Direct simulation was performed on a 96^3 grid.

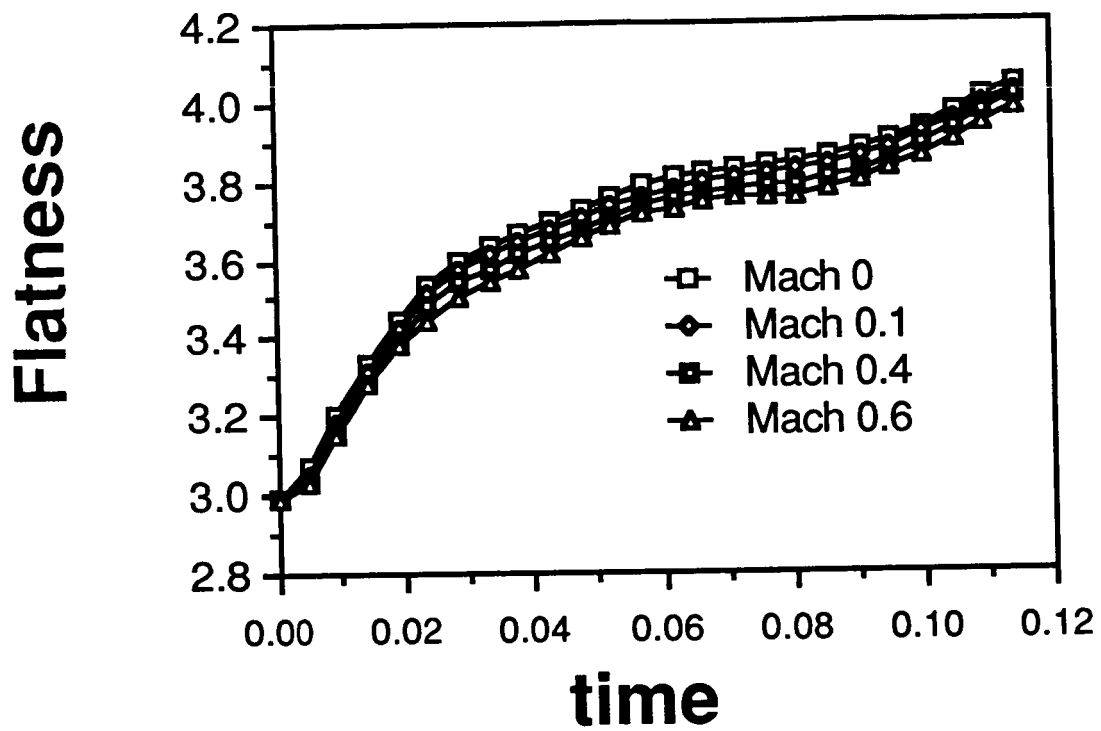


Fig. 6 Time history of one third the trace of F_l for M_0 of 0.0, 0.1, 0.4 and 0.6. Direct simulation was performed on a 96^3 grid.

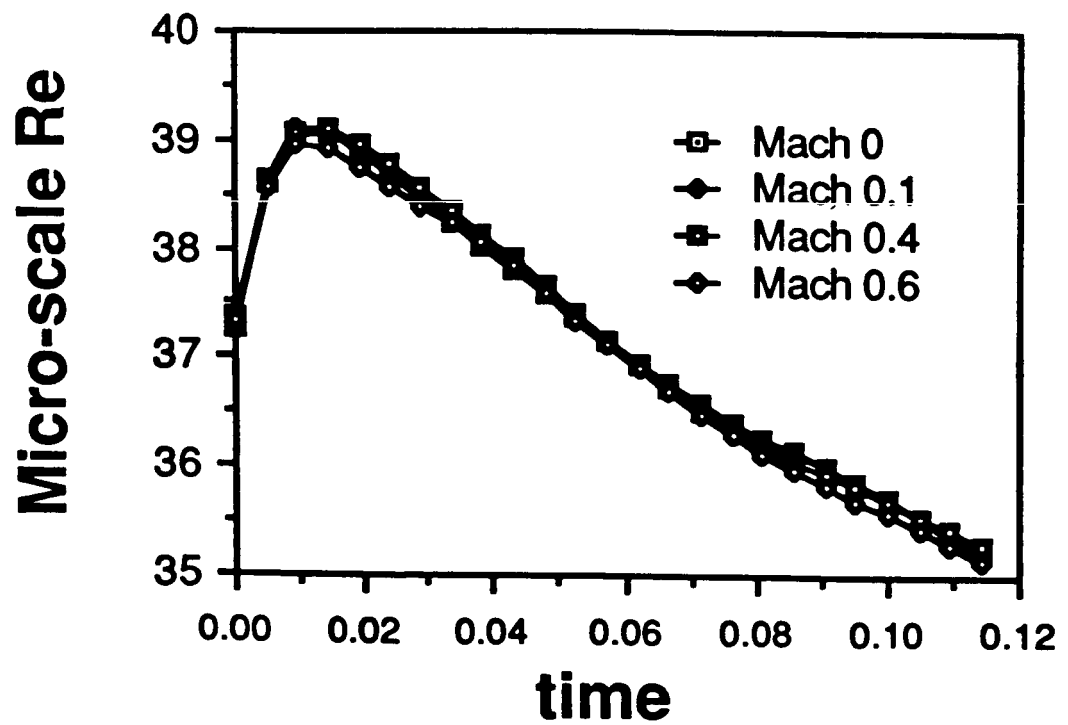


Fig. 7 Time history of one third the trace of R_λ for M_0 of 0.0, 0.1, 0.4 and 0.6. Direct simulation was performed on a 96^3 grid.

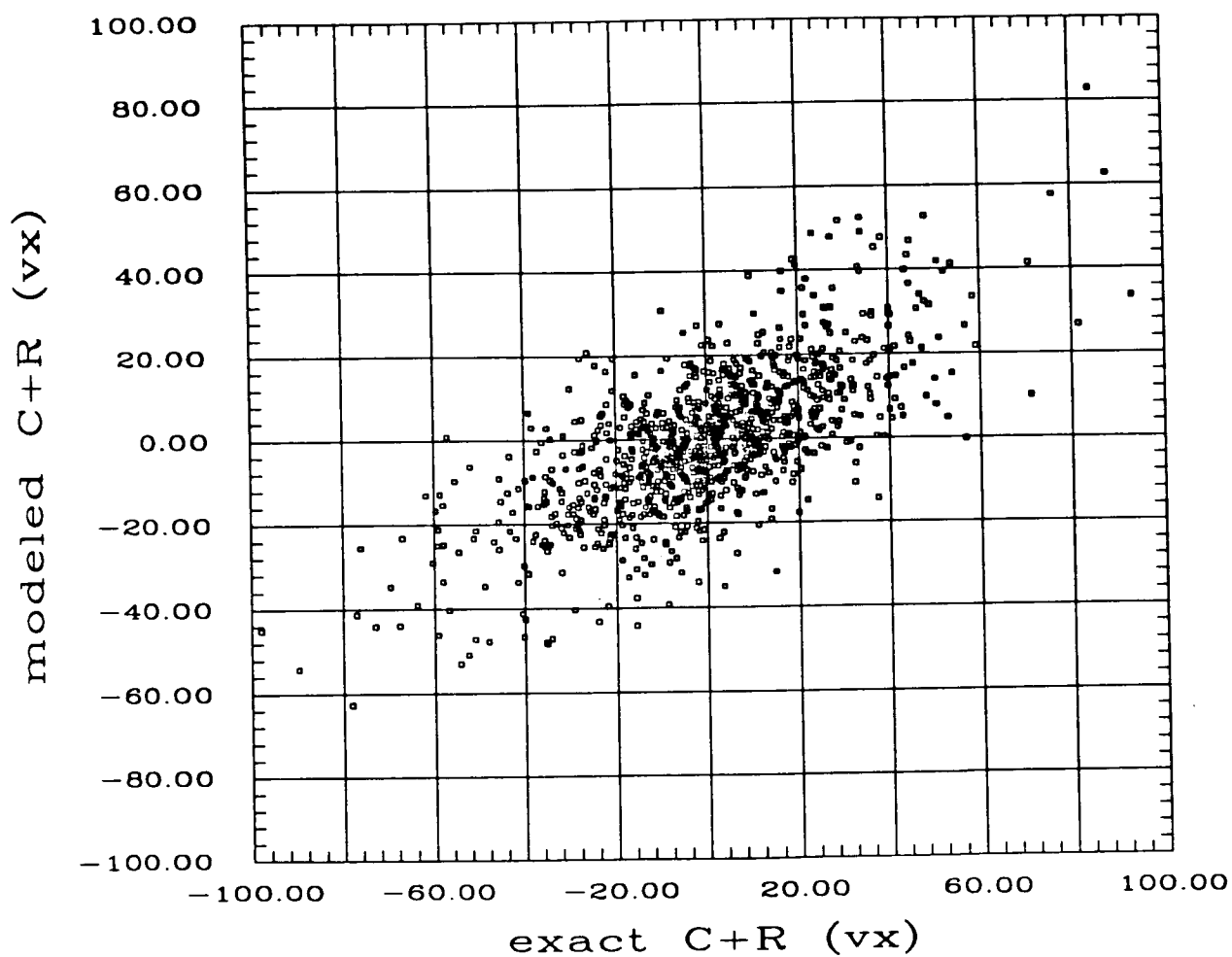


Fig. 8 Scatterplot of the x component of modeled $(C+R)^m$ versus $(C+R)^e$ on the vector level. Results are based on a direct simulation on a 96^3 grid and a data analysis on a 16^3 grid.

Standard Bibliographic Page

1. Report No. NASA CR-178273 ICASE Report No. 87-20		2. Government Accession No.		3. Recipient's Catalog No.	
4. Title and Subtitle TOWARD THE LARGE-EDDY SIMULATION OF COMPRESSIBLE TURBULENT FLOWS				5. Report Date March 1987	
				6. Performing Organization Code	
7. Author(s) G. Erlebacher, M. Y. Hussaini, C. G. Speziale, T. A. Zang				8. Performing Organization Report No. 87-20	
9. Performing Organization Name and Address Institute for Computer Applications in Science and Engineering Mail Stop 132C, NASA Langley Research Center Hampton, VA 23665-5225				10. Work Unit No.	
				11. Contract or Grant No. NAS1-18107	
12. Sponsoring Agency Name and Address National Aeronautics and Space Administration Washington, D.C. 20546				13. Type of Report and Period Covered Contractor Report	
				14. Sponsoring Agency Code 505-90-21-01	
15. Supplementary Notes Langley Technical Monitor: Submitted to J. Fluid Mechanics J. C. South Final Report					
16. Abstract New subgrid-scale models for the large-eddy simulation of compressible turbulent flows are developed based on the Favre-filtered equations of motion for an ideal gas. A compressible generalization of the linear combination of the Smagorinsky model and scale-similarity model (in terms of Favre-filtered fields) is obtained for the subgrid-scale stress tensor. An analogous thermal linear combination model is also developed for the subgrid-scale heat flux vector. The three dimensionless constants associated with these subgrid-scale models are obtained by correlating with the results of direct numerical simulations of compressible isotropic turbulence performed on a 96^3 grid using Fourier collocation methods. Extensive comparisons between the direct and modeled subgrid-scale fields are provided in order to validate the models. Future applications of these compressible subgrid-scale models to the large-eddy simulation of supersonic aerodynamic flows are discussed briefly.					
17. Key Words (Suggested by Authors(s)) subgrid-scale turbulence model, direct and large-eddy simulation, compressible Navier-Stokes equations			18. Distribution Statement 34 - Fluid Mechanics and Heat Transfer 64 - Numerical Analysis Unclassified - unlimited		
19. Security Classif.(of this report) Unclassified		20. Security Classif.(of this page) Unclassified		21. No. of Pages 38	
				22. Price A03	